EUROFUSION WPMST1-PR(16) 14728

K Verhaegh et al.

Spectroscopic investigations of volumetric recombination in the TCV divertor

Preprint of Paper to be submitted for publication in
22nd International Conference on Plasma Surface Interactions
in Controlled Fusion Devices (22nd PSI)

This work has been carried out within the framework of the EUROfusion Consortium and has received funding from the Euratom research and training programme 2014-2018 under grant agreement No 633053. The views and opinions expressed herein do not necessarily reflect those of the European Commission.

Spectroscopic investigations of divertor detachment in TCV

K.Verhaegh[a,b,*], B. Lipschultz[a], B.P. Duval[b], H. Reimerdes[b], C. Theiler[b], J. Harrison[c], B. Labit[b], R. Maurizio[b], C. Marini[b], F. Nespoli[b], U. Sheikh[b], C. Tsui[b,d], N. Vianello[e], W. Vijvers[f], TCV team, MST1 team

[a] *York Plasma Institute, Department of Physics, University of York, Heslington, York, YO10 5DD, United Kingdom*
[b] *Ecole Polytechnique Fdrale de Lausanne (EPFL), Swiss Plasma Center (SPC), CH-1015 Lausanne, Switzerland*
[c] *CCFE, Culham Science Centre, Abingdon, Oxon, OX14 3DB, United Kingdom*
[d] *University of California San Diego (UCSD), San Diego, CA, USA*
[e] *Corsorzio RFX, Corso Stati Uniti 4, 35127 Padova, Italy*
[f] *FOM Institute DIFFER, 5600 HH Eindhoven, The Netherlands*

Abstract

The aim of this work is to provide an understanding of detachment at TCV using spectroscopic measurements. A new Divertor Spectroscopy System has been developed for this purpose. Further development of Balmer line analysis techniques has allowed detailed information to be extracted on free-free and three-body recombination. During a density ramp a high density recombining region builds up at/near the outer divertor target, remaining there throughout the discharge. The density at the target (Langmuir probes) is a factor 5-6 higher with respect to the density derived from Stark broadening 5 cm above the target, implying a sharp density gradient near the target. At the highest core densities accessed (Greenwald fraction 0.7) the detachment front, where density is peaked, does not move more than a few cm poloidally from the target. At the same time density and recombination are rising all along the outer leg to the x-point, but still lower than near the target. The total inferred divertor recombination rate along the outer divertor leg reaches levels approaching the target ion flux as the target ion flux rolls over. The general characteristics of TCV detachment appear similar to other, higher density tokamaks although the extent of the recombination region appears poloidally extended and the drop in peak divertor ion current is not large.

Keywords: Detachment, Balmer line spectroscopy, volumetric recombination, tokamak power exhaust, TCV tokamak.

1. Introduction

For future fusion devices such as ITER, operating at least in a partially detached state is important for reducing the heat flux towards the divertor to below engineering limits (10 MW/m^2). Modelling for ITER demonstrates reduction of the peak heat flux near the separatrix by factors of up to 100 due to a number of atomic physics processes including line radiation, charge exchange and recombination. To address the need for further power removal before exhaust heat reaches the targets, which is needed for a DEMO fusion reactor and beyond, it behoves us to both understand the detachment process better.

The TCV tokamak is a medium-sized tokamak (R=0.89 m, a=0.25 m, B_t=1.4 T) well-suited for low density detachment studies.

There has been considerable work utilizing spectroscopic measurements for understanding detachment, where the characteristics of the recombining region are extracted from the Balmer series emission [1, 2, 3, 4, 5]. The total amount of ion loss due to volumetric recombination in the divertor can then be compared with the total ion particle flux reaching the target [1].

The aim of this study is to develop a detailed understanding of the detachment process at TCV where low densities should give us insight into how the role of recombination changes. The results presented will emphasize spectroscopic measurements which will be compared with data from Langmuir probes and bolometry. For this investigation, a new spectroscopic diagnostic has been developed for the TCV divertor, enhancing TCV's edge diagnostic capabilities. Improvements in interpretation of Balmer series signals have been developed for extracting information on recombination on electron temperature.

Using spectroscopic measurements we will show that the observed recombination region during a density ramp builds up at the target in the TCV divertor and remains strongest near the target throughout the discharge, which contrasts the "typical" picture of detachment where the recombining region moves towards the x-point during a density ramp.

2. Experimental setup

2.1. TCV's Divertor Spectroscopy System (DSS)

The primary measurements of the recombination characteristics are made using a new spectrometer with views of the divertor, which we refer to as the DSS. The viewing optics provide a poloidal, line-integrated, view of the divertor which is imaged through a quartz window onto 32×400μm HOH silica-clad fibres, yielding 32 lines of sight (figure 1). The fibres of each system are coupled to a Princeton Instruments Isoplane SCT 320 spectrometer with a 30 μm entrance slit, coupled to an Andor iXon Ultra 888 EMCCD camera with a 1024 x 1024 pixel sensor, digitized at 30 MHz with 16 bit resolution and a frame transfer buffer. The spectrometer is a mirror based Schmidt-Czerny-Turner spectrometer with minimized aberrations and contains a grating turret with 1800 l/mm, 600 l/mm and 300

*Corresponding author
Email address: kevin.verhaegh@epfl.ch (K.Verhaegh)

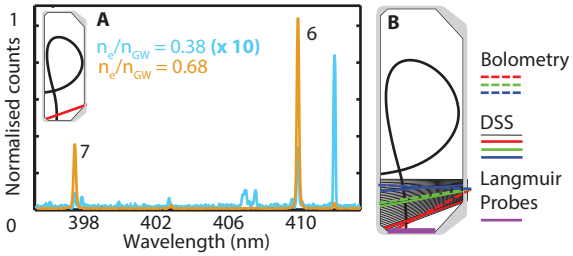

Figure 1: Example Balmer line spectra, averaged over 100 ms, measured by DSS near the target for two different spectral ranges at two different core densities.

l/mm gratings, yielding a measured FWHM resolution of 0.06, 0.22 and 0.44 nm and a spectral range of 19, 63 and 131 nm, respectively. The 1800 l/mm grating was typically utilized to allow n_e measurements through Stark broadening of the n=6,7 Balmer series lines.

The system has been absolutely calibrated in intensity and wavelength. A stray light correction technique [6] has been applied to reduce the stray light induced during the absolute intensity calibration measurement. Our analysis has found the measurement inaccuracy in the absolute Balmer line intensities to be $\sim$10%.

The central part of each fiber image on the CCD is sampled with a 'region of interest' (ROI) with negligible optical cross-talk. The CCD sensor is cooled to -70 C using a water cooled Peltier cooler in order to minimize the dark noise. A dark frame is acquired before and after the plasma discharge, which is subtracted from the measurements. The spectroscopic measurements are susceptible to read-out smear of the CCD [7] whereby each ROI spends time integrating light from other ROIs as it is transferred to the optically dark frame-transfer region. The spectra are corrected for smearing by post-processing using a numerical matrix-based algorithm. This algorithm is based on the row-shift (frame transfer) time and integration time, as described in [7] and assumes that the light incident on the CCD is approximately constant over the frame transfer time (1.15 ms). Tests, utilizing a time-stabilized source, show that this numerical algorithm predicts the amount of smearing within 10 % of the observed amount of smearing.

The measured spectra are acquired with an acquisition frequency of 100 - 200 Hz. For the results analysed in this work, the measured spectra have been re-sampled by averaging frames and/or ROIs over the entire discharge, taking into account changes in the instrumental function when averaging over ROI. This greatly improves the S/N ratio in the attached phase where the Balmer line emission ($n>5$) is low, improving the determination of n_e from line fitting (section 2.3).

Figure 1A indicates the observed intensity of medium-n Balmer lines ($n=6,7$) increases greatly during the density ramp. The observed spectra corresponds to the view line close to the target highlighted in figure 1B (red), where all the diagnostic locations used in this work are shown.

2.2. Extracting information on recombination from Balmer lines using a collisional-radiative model

The brightness ($B_{n\to2}$ in [photons $m^{-2}s^{-1}$]) of a hydrogen Balmer line with quantum number n can be modelled using the Photon Emissivity Coefficients (PEC) [photons m ^{3}s $^{-1}$] as indicated in equation 1, which contains a recombination and excitation part: $B^{rec,exc}_{n\to2}$. It is assumed that all line emission comes from a region with width ΔL with homogeneous electron density n_e, homogeneous electron temperature T_e and homogeneous neutral density n_o. The effect of these assumptions are discussed in section 2.4. Additional assumptions are that hydrogen collisional radiative model results are valid for deuterium and that the contribution of charge exchange and molecular reactions to the emission of a certain Balmer line is negligible. The PEC for the corresponding $n\to2$ transition for recombination and excitation ($PEC^{rec,exc}_{n\to2}$() are obtained from the Open-ADAS database [8] and have been calculated using the ADAS collisional-radiative model [9].

$$B_{n\to2}=\underbrace{\Delta L n_e^2 PEC^{rec}_{n->2}(n_e,T_e)}_{B^{rec}_{n\to2}}+\underbrace{\Delta L n_o n_e PEC^{exc}_{n->2}(n_e,T_e)}_{B^{exc}_{n\to2}} \quad (1)$$

For further discussion we define F_{rec} as the fraction of total Balmer line radiation due to recombination ($F_{rec}(n)=B^{rec}_{n\to2}/B_{n\to2}$) and we define F_{76} as the ratio of brightness of the $7\to2$ and $6\to2$ Balmer lines ($F_{76}=B_{7\to2}/B_{6\to2}$). Although the analysis in this section is mainly focused on the $n=6,7$ Balmer lines, the analysis strategy is general and can be applied to other Balmer lines.

2.2.1. Using Balmer line ratios to obtain the fraction of Balmer line emission due to recombination

We have developed a method for separating the recombination and excitation part from the Balmer line emission, which can be particularly important for analysing medium-n $n=6,7$ Balmer lines.

In figure 2A, the calculated F_{76} is shown as function of temperature for $n_e=5.10^{19}m^{-3}$ and various values of n_o/n_e, which is insensitive to density and differs by $<5\%$ in the range $n_e=10^{19}-10^{20}m^{-3}$. When assuming the neutral fraction (n_o/n_e) is constant, F_{76} transitions from the $B_{6,7\to2}\approx B^{exc}_{6,7\to2}$ limit at high T_e to the $B_{6,7\to2}\approx B^{rec}_{6,7\to2}$ limit at low T_e where F_{76} is $\sim$ twice as high. The temperature at which this transitioning occurs depends on n_o/n_e, since n_o serves as a weighting factor for $B^{exc}_{n\to2}$.

Simulations indicate that n_o/n_e can reach 0.1 [10]. In addition, divertor pressure measurements with an absolutely calibrated baratron gauge indicate n_o/n_e rises from order 10^{-3} to 0.05 at the lowest T_e, which is supported by OSM-Eirene modelling results [11].

$F_{rec}(n)$ for the $n=6,7,9$ Balmer lines has a one to one relationship with F_{76} (figure 2B) for a large range of $F_{rec}(n=6,7)$. Changing n_o/n_e by a factor 100 results in a $F_{rec}(n)$ change <0.1. For a certain fixed F_{76}, $F_{rec}(n)$ is larger for higher-n Balmer lines, which are hence more suitable for recombination studies. When calculating the recombination rate (section 2.2.2) and T_e

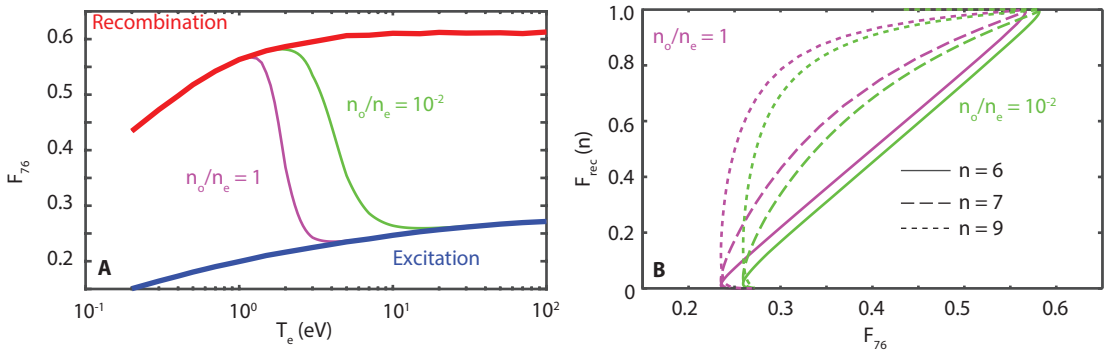

Figure 2: **A**: Modelled F_{76} as function of T_e for multiple n_o/n_e for n_e=5.10$^{19}m^{-3}$. **B**: Relation between F_{76} and $F_{rec}(n$=6,7,9).

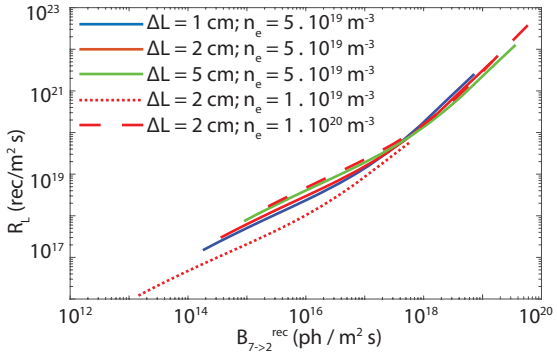

Figure 3: Relation between the line integrated volumetric recombination rate and the modelled $B^{rec}_{7\to2}$ for a range of different n_e and ΔL.

(section 2.2.3) from $B_{6\to2}$ using $F_{rec}(n$=6) the result is within 5 % of when $B_{7\to2}$ is used along $F_{rec}(n$=7), providing evidence that the $F_{rec}(n)$ calculation is correct.

Therefore, by measuring F_{76} we can obtain $F_{rec}(n)$ using the relation shown in 2B. Although the n_e dependence of F_{rec} is weak, we use the n_e obtained from Stark broadening and we assume n_o/n_e=0.1. By multiplying the measured $B_{6,7\to2}$ with $F_{rec}(n$=6,7), determined from the measured F_{76} we obtain $B^{rec}_{6,7\to2}$.

2.2.2. Obtaining line integrated volumetric recombination rates from absolute Balmer line intensities

We have developed a method for calculating recombination rates, which has the advantage over previous work [12] that no direct temperature estimate is required in the calculation for obtaining the recombination / photon ratio. n_e, which can be acquired from the Balmer line shape (section 2.3)), and a ΔL estimate is required.

We start by obtaining the number of recombinations per photon as in [13] for a particular Balmer line using Open-ADAS, which is (assuming the plasma is optically thin) the ratio of the ADAS effective recombination rate coefficient ($ACD(n_e,T_e)$), which takes into account both radiative and three body recombination, and the ADAS $PEC^{rec}_{n\to2}(n_e,T_e)$. The effect of molecular assisted recombination is neglected, which generally does not have a strong effect in the divertor [13, 1]. However, recent work has shown that molecular assisted recombination might have a significant effect on detachment in relatively low density plasmas [14]. By multiplying the number of recombinations per emitted photon with $B^{rec}_{n\to2}$, we obtain the line integrated volumetric recombination rate, which we refer to as $R_L(n_e,T_e,\Delta L)$ [rec /m^{2}s].

By investigating how the relation R_L and $B^{rec}_{n\to2}$ varies as a function of T_e with fixed n_e, ΔL, a one to one relationship is obtained (figure 3) which only depends weakly on n_e and ΔL. We have determined ΔL as the $1/e$ fall-off length of the n_e profile at the target measured by Langmuir probes in the attached phase, which is mapped along the field lines towards the x-point to determine ΔL for each point where the DSS view line intersects with the separatrix. Hence, by determining $B^{rec}_{n\to2}$ from $B_{n\to2}$ and $F_{rec}(n)$, the line integrated volumetric recombination rate can be determined.

The measurement inaccuracy of the recombination rate is estimated at $\sim$30%, which is calculated using measurement uncertainties in n_e, $B_{n\to2}$ and F_{rec}. The obtained line integrated volumetric recombination rate is insensitive to profile effects (section 2.4). A similar approach as described in this section could be used to obtain line integrated excitation rates, which can be used to track the excitation region.

2.2.3. Obtaining T_e from absolute intensity measurements

We have developed a new method for calculating a line averaged T_e from a measured line intensity, which is averaged over the region of the line integral where $B^{rec}_{n\to2}$ is the largest. This has the advantage that only the absolute intensity of a single spectral

line is required during the calculation.

The $PEC^{rec}_{n\to2}(n_e,T_e)\approx PEC^{rec}_{n\to2}(T_e)$ has a strong temperature dependence (its n_e dependence is $<5\%$ for $n>6$ Balmer lines in a density range $n_e=10^{19}-10^{21}\mathrm{m}^{-3}$). By using the Stark broadened measured n_e and assuming a certain ΔL, the electron temperature can be obtained by solving $B^{rec}_{n->2}=\Delta L n_e^2 PEC^{rec}_{n->2}(T_e)$, which results in a line averaged temperature. This method requires a high accuracy in the $B^{rec}_{n->2}$ and hence is only applicable when $F_{rec}(n)\sim1$. The line averaged temperature is sensitive to assumptions on ΔL and is therefore susceptible to profile effects (section 2.4). Therefore, this measurement should be used as an indicator for trends in T_e, instead of an absolute T_e measurement.

2.3. Obtaining n_e from Stark broadening

Spectral lines emitted by plasmas are broadened by Stark broadening, which provides a line averaged measurement of the electron density [15, 4], weighted towards the high n_e region (section 2.4). Assuming that all line emission comes from a slab of plasma with homogeneous n_e,T_e, Stark broadening of a Balmer line can be expressed as a modified Lorentzian [4]:

$$L_S(\lambda,\lambda_0,T_e,n_e,n)=\frac{A}{(\lambda_0-\lambda)^{5/2}+(\frac{1}{2}C_{n\to2}\frac{n_e^{a_{n\to2}}}{T_e^{b_{n\to2}}})^{5/2}} \tag{2}$$

This equation serves as a a parametrization of the Model Microfield Method Stark model [16], where $C_{n\to2}$, $a_{n\to2}$ and $b_{n\to2}$ are coefficients provided for several Balmer lines [4], λ_0 is the peak location of the fit in nm, λ is the wavelength in nm and A is a normalization constant. Since $a_{n\to2}\gg b_{n\to2}$, Stark broadening is more strongly dependent on n_e than T_e.

The spectrometer induces additional instrumental broadening to the emitted spectral line, which is best described by a Lorentzian for our spectrometer. Coma leads to a skewed instrumental function and hence the instrumental line is parametrized by a modified asymmetric Lorentzian:

$$L_I(\lambda_0,\lambda,p,a,b)\propto\left\{\begin{array}{ll}(\frac{1}{1+4(\frac{\lambda-\lambda_0}{p})^2})^a, & \text{for } \lambda\le\lambda_0\\ (\frac{1}{1+4(\frac{\lambda-\lambda_0}{p})^2})^b, & \text{for } \lambda\ge\lambda_0\end{array}\right\} \tag{3}$$

Coefficients a, b and p are obtained for each CCD ROI separately at multiple wavelengths and multiple horizontal positions by fitting the measured instrumental line shape from a spectral lamp.

The experimentally observed Balmer line shape is fitted using a numerical algorithm based on Gradient Expansion Algorithm [17]. The used fitting function is the convolution of Stark broadening (equation 2), Doppler broadening [15] and the instrumental broadening (equation 3). Magnetic effects (Zeeman splitting) are neglected.

In the fitting routine, the free parameters are the location of the line λ_0, the peak intensity of the measured line and the electron density. To lower the amount of fitting parameters, it is assumed $T_e=3$ eV for the Stark broadening and $T_i=3$ eV for the Doppler broadening. The sensitivity of this assumption has been investigated by generating spectral lines ($7\to2$) with various T_e,T_i and fitting the resulting synthetic spectral line with a Stark model which assumes $T_e=T_i=3$ eV. When varying T_e between [0.2−15] eV, the differences obtained in density from the Stark fit are $<0.1\%$. When varying T_i between [0.2−15] eV, the density obtained from the fits are over-estimated ($<5\%$) for $T_i=15$ eV and under-estimated ($<10\%$) for $T_i=0.2$ eV.

The main parameter leading to measurement error in the Stark inferred density (n_e^{Stark}) is the signal/noise (S/N) level. The effect of the S/N level on n_e^{Stark} has been investigated using a Monte-Carlo approach, where 100 spectral lines are simulated using a fixed value for n_e including a level of white noise. Each simulated line is fitted, taking into account instrumental broadening, providing a n_e^{Stark} distribution, which can be approximated by a normal distribution whose peak corresponds to the fixed n_e and whose standard deviation provides the measurement uncertainty of n_e^{Stark} as function of S/N level and n_e. Since Stark broadening is stronger for higher-n Balmer lines, using higher-n Balmer lines for Stark fitting leads to decreased measurement error. The instrumental function for edge ROIs of the CCD (which correspond to edge chords) are up to twice as wide as the instrumental function for the central chord, resulting in higher measurement error.

2.4. Investigating profile effects on n_e (Stark), T_e and recombination measurements

The sensitivity of the n_e (Stark), T_e and recombination measurements on profile effects has been investigated by using various a priori n_e, T_e and n_o profiles, including hollow, flat and peaked (Gaussian) profiles with a width varying from 0.5 - 7 cm. For peaked profiles, peak densities $n_{e,0}=[3,5,10].10^{19}$ m^{-3} and corresponding peak temperatures $T_{e,0}=[15,3,1]$ eV have been assumed. A flat neutral density profile using $n_o=[10^{18},10^{19}]$ m^{-3} has been assumed.

Using these profiles, the Balmer line emission is modelled at every point of the profile and the corresponding Stark line shape is calculated. The Stark line shapes, weighted by the Balmer line emission, is summed over all points of the profile and the n_e^{Stark}, R_L and T_e is inferred from the obtained Balmer line spectrum using the methods described in sections 2.2 and 2.3. Points on the profile with $T_e<0.2$ eV have not been taken into account since they fall outside the range of our Open-ADAS grid.

Assuming peaked n_e profiles, n_e^{Stark} obtained from the synthetic spectra is in between 65 - 100 % of the peak density value $n_{e,0}$. The largest deviation between n_e^{Stark} and $n_{e,0}$ occurs for $\lambda_{n_e}\approx\lambda_{T_e}$, for which n_e^{Stark} is within 65−70% of $n_{e,0}$, independently of L_0.

R_L obtained from the synthetic spectrum deviates $<5\%$ from R_L obtained by integrating the local recombination rate over the profile, except for cases with a strongly hollow n_e profile where the synthetic spectrum can be underestimated by up to 50 %.

For peaked T_e profiles with sufficiently low peak $T_{e,0}$ (¡ 2 eV), the T_e obtained from the synthetic spectrum is generally in between 50 - 100 % of $T_{e,0}$.

3. Experimental results

In this section we will use the DSS data and analysis techniques described in section 2 to illustrate how divertor conditions vary as detachment proceeds in TCV. Connections will be made to other diagnostic measurements to form a more complete picture of the detachment process. Our observation is that some of the characteristics of detachment on TCV and other, higher density, tokamaks are similar. However, detachment in TCV does not lead to strong drops in density and large movement of the recombination region.

3.1. Onset, evolution and dynamics of detachment

A reference plasma discharge is utilized for illustrating the process of detachment in TCV (#52065). It has a single null magnetic divertor geometry with a plasma current of 340 kA and has a reversed toroidal field direction (∇B away from the x-point). The spectroscopic data has been acquired at 200 Hz and has been averaged over 2 ROIs and a number of time frames, as indicated in the legends figure 4 to improve S/N level. The line colour and line style shown in figure 4A-J corresponds to the diagnostic locations shown in figure 1B. Similar detachment characteristics as observed for #52065 have been found for $\sim$20 other density ramp discharges, although both the core density at which each characteristic occurs, magnitude of recombination and magnitude of J_{sat} drop varies between different discharges.

During the ramp in core density, represented by the line averaged density normalised over the Greenwald density $<n_e>/n_G$ in figure 4A), the trend of F_{76} (figure 4C) is consistent with a decreasing temperature as predicted in figure 2. This results in an increase in $F_{rec}(n=7)$ from $\sim$0 to $\sim$1 (figure 4H), over a considerable increase in core density from $\overline{n_e}/n_G=0.4$ to $\overline{n_e}/n_G=0.6$), which first occurs at the target and later expands towards the x-point, indicating an expansion of the recombining region.

All the various spectral features are consistent with a strong recombining region near the target. The strong increase in $B_{6,7\rightarrow2}$ (figure 4B), combined with a rising $F_{rec}(n=7)$, implies that the R_L (figure 4F) is strongly increasing. Similar to trends in F_{76}, the onset of this non-linear increase starts first close to the target and later increases closer to the x-point. The increase in $B_{7\rightarrow2}$ during the density ramp is both due to the n_e increase (figure 4D) and T_e decrease (obtained from $B_{7\rightarrow2}$ when $F_{rec}(n=7)>0.5$ - figure figure 4D).

Our results suggest that recombination is insufficient to effectively reduce the density close to the target. After $F_{rec}(n=7)\rightarrow1$, both $B_{6,7\rightarrow2}$ and n_e (Stark) keep increasing until the end of the discharge while remaining highest at the target, resulting in the R_L being the strongest near the target (figure 4F) throughout the discharge. At first glance this would seem to indicate that while ionization and impurity radiation have detached from the target, the high density region has not.

It is possible that the inferred R_L is an underestimate. Since the closest target DSS view line intersects the separatrix 5 cm above the strike point we are not monitoring the recombination signatures in a region where the recombination rate could be higher. If the recombination spatial profile is extrapolated to the target, the line integrated recombination rate at the target is three times higher than at the position of the DSS view 5 cm above the target. However, target probe measurements (figure 4D) indicate n_e drops in this non-observed region, which in turn would lower lower the recombination. In addition, the lower density at the target compared to 5 cm poloidally upstream indicates that the high-density recombination front has moved off the target a short distance. Detachment in TCV has so far never reached the level where the high density recombination region reaches the x-point.

The total recombination rate in the divertor R_V [rec./s] is determined by integrating R_L toroidally and poloidally across the chords. R_V increases strongly during the last phase of the discharge (figure 4G), and reaches values of up to $R_V=(9.0\pm0.35).10^{21}$ rec/s, which is $\sim$20% of the total particle flux measured by Langmuir probes at that time. Note that if we apply the above mentioned extrapolation of the recombination rate to the target the total recombination rate could increase by up to 45 %. Although the particle flux measured by the Langmuir probes drops for $t>1.0$ s, R_V at that time is relatively low, which indicates that recombination losses are not the main contributor to the $J_{\rm sat}$ drop initially. However, at later times, the recombination rate can contribute considerably to the particle flux drop.

3.2. Recombination signatures compared with other diagnostics information

Combining data from the DSS and divertor target Langmuir probe data is informative about the development of detachment. The peak target electron density determined from Langmuir probe (LP) I-V characteristics is in agreement with n_e^{Stark} near the target until 0.9 s (figure 4I), which is close to the time when $B_{6,7\rightarrow2}$ starts increasing strongly. Across many tokamaks it has been found that the temperature derived from Langmuir probes is overestimated for $T_e<5$ eV, [18, 19]. Assuming this is also true for TCV, we utilize J_{sat} and n_e^{Stark} (5 cm from the target) to calculate $T_e^{\rm mod}$ (figure 4E). $T_e^{\rm mod}$ decreases during the density ramp in agreement with the Balmer line derived T_e up untill 0.9 s when the target particle flux. Past that time T_e^{mod} is lower than the Balmer-derived T_e, most likely because the density in two locations (DSS chord and probe) differ. After 0.9 s also n_e (LP) start to drop, while n_e^{stark} 5 cm away poloidally continues to increase. The over-estimate of T_e (LP) influences the n_e (LP) measurement. Even when taking this effect into account by using J_{sat} and the Balmer-line derived T_e to determine $n_e^{\rm mod}$, the $n_e^{\rm mod}$ drops at the same time n_e (LP) drops, which indicates that the drop in n_e (LP) is not an artefact of the T_e overestimation.

The concentration of total radiation in the divertor moves from the target towards the x-point ahead of signatures in the recombining region. In figure 4E the line integrated emissivity obtained from bolometric measurements is shown for the three bolometer view lines which are closest to the three shown DSS view lines. The radiation near the target peaks at 0.85 s, after which the radiation front moves towards the x-point until 1.05 s. The movement of the radiation front is correlated with $F_{76}\approx0.35$, suggesting that the movement of the radiation front is correlated with the appearance of recombination signatures.

The integrated power load to the outer strike point as determined by Langmuir probes, shown in figure 4J, goes up until 0.85 s as a result of the Ohmic power increase during the density ramp, after which it starts dropping. The onset of the decrease of power load is correlated with the radiation peaking near the target and the appearance of recombination signatures.

4. Discussion

The onset of detachment observed spectroscopically at TCV is generally similar to the dynamics previously observed at higher density machines, but there are also significant differences.

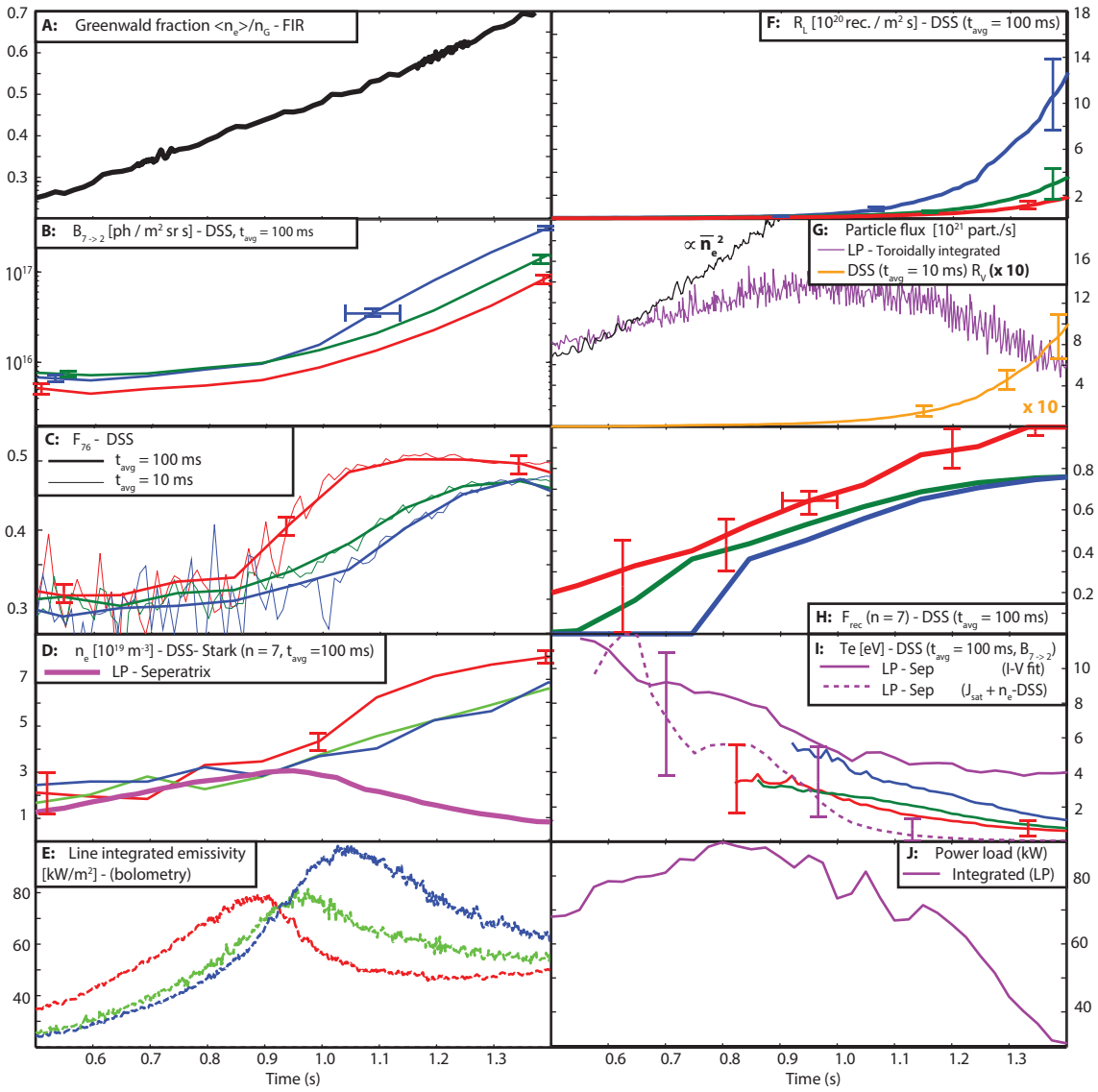

Figure 4: Temporal evolution of several quantities measured by DSS and derived using DSS data for three view lines during a single null density ramp shot (52065). In addition, data obtained from Langmuir probes (LP) and bolometry is shown. The colours of the plot indicate the measurement locations shown in figure 1B.

As the core density is increased in L-mode plasmas, the target density increases and the temperature decreases, which are general characteristics of a high-recycling divertor. However, the ion current to the target does not increase $\propto < n_e >^2$ as expected from the two point model (assuming $n_{e,up} \propto < n_e >$) [20] (figure 4G). This difference to other, high density machines and the 2-point model may be due to the fact that the ionization mean free path in TCV ($\lambda_{ioniz} \sim 5-10$ cm) is larger compared to the width of the divertor plasma ($d_{fan} \sim$ a few cm) near the target [10]. Together with the open nature of the divertor, neutrals are not well-confined, thus leading to less ionization and a slower rise in divertor density. That slows down the rise in charge exchange and recombination processes, thus slowing down the detachment process.

Once the detachment process starts with the drop in divertor target density and the rise in recombination signatures (figures 4G and 4C) the process of detachment proceeds slowly. Instead of a swift movement of the recombination and high-density regions, observed at other high density machines [1, 5], the recombining region and peak density stays near the target at TCV while recombination signatures (e.g. F_{76} in figure 4C and R_L in figure 4F) extend towards the x-point. At the highest core and divertor densities in the TCV plasmas studied so far, the drop in target density (figure 4D) concurrent with the continued increase in the DSS-inferred density indicates that the detachment region (in the sense of both low density and low temperature) has moved off the target slightly, less than the 5 cm corresponding to the lowest DSS chord. However, that movement is very slow given that the Stark-derived density continues to rise throughout the remainder of the discharge.

The inference of recombination rates through the DSS data analysis also provide some insight into the role of recombination in removing ions from the plasma and causing a density drop. As discussed earlier, recombination remains highest near the target throughout the discharge, with the total amount of recombination rising rapidly to levels at the end of the discharge compatible to the target ion flux. Given that the target density drops earlier in the pulse, the question is whether recombination is playing

an important role at that time. The two possibilities are that the ion source upstream could start dropping at the same time as the target density falls. Or, that the recombination local to the flux tube of the peak ion flux is removing significant ion flux. We do not have enough spatial information at this time to comment further on the relative important of the two effects. The total recombination rate only reaches 10 % of the total target ion flux at the latest stages of the discharge, which again raises questions of whether recombination is playing a significant role in reducing the target ion flux.

5. Summary

The physics of the TCV divertor, including the detached regime, has been investigated at TCV, using a newly developed divertor spectroscopy system (DSS), together with advancements in techniques for extracting information from the Balmer spectrum. Analysis of the DSS data has been instrumental in characterizing the behaviour of detachment in TCV. We find that the detachment process develops slowly: the radiation first peaks near the divertor and then moves towards the x-point. The rise in the dominance of recombination signatures over excitation follows the movement of the radiation peak, while the strongest level of density and recombination remains close to the target. Even as the plasma density above the target continues to increase the density and ion current to the target drop implying that the detached, low pressure and density region has moved off the target. But within the density range studied on TCV, the detachment front moves no further.

The role of recombination in ion loss has been investigated. We find that there is no clear connection between the ion current drop at the target and the level of recombination and further studies are needed.

6. Acknowledgments

This work has been carried out within the framework of the EUROfusion Consortium and has received funding from the Euratom research and training programme 2014-2018 under grant agreement No 633053. The views and opinions expressed herein do not necessarily reflect those of the European Commission.

References

[1] B. Lipschultz, J. Terry, C. Boswell, J. Goetz, A. Hubbard, S. Krasheninnikov, B. LaBombard, D. Pappas, C. Pitcher, F. Wising, et al., The role of particle sinks and sources in alcator c-mod detached divertor discharges, Physics of Plasmas.

[2] G. McCracken, M. Stamp, R. Monk, A. Meigs, J. Lingertat, R. Prentice, A. Starling, R. Smith, A. Tabasso, Evidence for volume recombination in jet detached divertor plasmas, Nuclear fusion 38 (4) (1998) 619.

[3] A. Meigs, S. Brezinsek, M. Clever, A. Huber, S. Marsen, C. Nicholas, M. Stamp, K.-D. Zastrow, J. E. Contributors, Deuterium balmer/stark spectroscopy and impurity profiles: first results from mirror-link divertor spectroscopy system on the jet iter-like wall, Journal of Nuclear Materials 438 (2013) S607–S611.

[4] B. Lomanowski, A. Meigs, R. Sharples, M. Stamp, C. Guillemaut, J. Contributors, Inferring divertor plasma properties from hydrogen balmer and paschen series spectroscopy in jet-ilw, Nuclear Fusion 55 (12) (2015) 123028.

[5] S. Potzel, M. Wischmeier, M. Bernert, R. Dux, H. Müller, A. Scarabosio, et al., A new experimental classification of divertor detachment in asdex upgrade, Nuclear Fusion 54 (1) (2014) 013001.

[6] E. Kristensson, J. Bood, M. Alden, E. Nordström, J. Zhu, S. Huldt, P.-E. Bengtsson, H. Nilsson, E. Berrocal, A. Ehn, Stray light suppression in spectroscopy using periodic shadowing, Optics express 22 (7) (2014) 7711–7721.

[7] A. A. Dorrington, M. J. Cree, D. A. Carnegie, The importance of ccd readout smear in heterodyne imaging phase detection applications, in: Proc. Image and Vision Computing New Zealand, Citeseer, 2005, pp. 73–8.

[8] Open-adas; open - atomic data analysis structure [online].

[9] H. Summers, Atomic data and analysis structure, JET Report.

[10] M. Wischmeier, Simulating divertor detachment in the tcv and jet tokamaks, EPFL.

[11] J. Harrison, W. Vijvers, C. Theiler, B. Duval, S. Elmore, B. Labit, B. Lipschultz, S. Lisgo, C. Tsui, H. Reimerdes, U. Sheikh, K. Verhaegh, M. Wischmeier, the MST1 team, the TCV team, Recent detachment studies on the tcv tokamak, Journal of Nuclear Materials and Energy this issue.

[12] J. L. Terry, B. Lipschultz, A. Y. Pigarov, S. Krasheninnikov, B. LaBombard, D. Lumma, H. Ohkawa, D. Pappas, M. Umansky, Volume recombination and opacity in alcator c-mod divertor plasmas, Physics of Plasmas (1994-present) 5 (5) (1998) 1759–1766.

[13] J. L. Terry, B. Lipschultz, A. Y. Pigarov, S. Krasheninnikov, B. LaBombard, D. Lumma, H. Ohkawa, D. Pappas, M. Umansky, Volume recombination and opacity in alcator c-mod divertor plasmas, Physics of Plasmas (1994-present) 5 (5) (1998) 1759–1766.

[14] A. Kukushkin, S. Krasheninnikov, A. Pshenov, R. D., Role of molecular effects in divertor plasma recmbination, 2016.

[15] H.-J. Kunze, Introduction to plasma spectroscopy, Vol. 56, Springer, 2009.

[16] C. Stehlé, R. Hutcheon, Extensive tabulations of stark broadened hydrogen line profiles, Astronomy and Astrophysics Supplement Series 140 (1) (1999) 93–97.

[17] P. R. Bevington, D. K. Robinson, Data reduction and error analysis, McGraw-Hill.

[18] O. Batishchev, S. Krasheninnikov, P. J. Catto, A. Batishcheva, D. Sigmar, X. Xu, J. Byers, T. Rognlien, R. Cohen, M. Shoucri, et al., Kinetic effects in tokamak scrape-off layer plasmas, Physics of Plasmas (1994-present) 4 (5) (1997) 1672–1680.

[19] O. Batishchev, X. Xu, J. Byers, R. Cohen, S. Krasheninnikov, T. Rognlien, D. Sigmar, Kinetic effects on particle and heat fluxes in detached plasmas, Physics of Plasmas (1994-present) 3 (9) (1996) 3386–3396.

[20] P. Stangeby, The plasma boundary of magnetic fusion devices, The Plasma Boundary of Magnetic Fusion Devices. Series: Series in Plasma Physics, ISBN: 978-0-7503-0559-4. Taylor & Francis, Edited by Peter Stangeby, vol. 7 7.